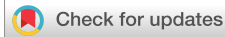


RESEARCH ARTICLE | NOVEMBER 18 2024

## Exploration of contact angle hysteresis mechanisms: From microscopic to macroscopic

Hongmin Zhang ; Haodong Zhang ; Fei Wang  ; Britta Nestler 



*J. Chem. Phys.* 161, 194705 (2024)

<https://doi.org/10.1063/5.0232287>



### Articles You May Be Interested In

Effect of wall free energy formulation on the wetting phenomenon: Conservative Allen–Cahn model

*J. Chem. Phys.* (October 2023)

Particle size effect on surface/interfacial tension and Tolman length of nanomaterials: A simple experimental method combining with theoretical

*J. Chem. Phys.* (May 2024)

Molecular interactions at the metal–liquid interfaces

*J. Chem. Phys.* (June 2022)



The Journal of Chemical Physics

## Special Topics Open for Submissions

[Learn More](#)

# Exploration of contact angle hysteresis mechanisms: From microscopic to macroscopic

Cite as: *J. Chem. Phys.* **161**, 194705 (2024); doi: [10.1063/5.0232287](https://doi.org/10.1063/5.0232287)

Submitted: 6 August 2024 • Accepted: 31 October 2024 •

Published Online: 18 November 2024



View Online



Export Citation



CrossMark

Hongmin Zhang,<sup>1</sup>  Haodong Zhang,<sup>1,2</sup>  Fei Wang,<sup>1,2,a)</sup>  and Britta Nestler<sup>1,2,3</sup> 

## AFFILIATIONS

<sup>1</sup>Institute of Nanotechnology, Karlsruhe Institute of Technology, Hermann-von-Helmholtz Pl. 1, 76344 Eggenstein-Leopoldshafen, Germany

<sup>2</sup>Institute for Applied Materials - Microstructure Modelling and Simulation (IAM-MMS), Karlsruhe Institute of Technology (KIT), Straße am Forum 7, 76131 Karlsruhe, Germany

<sup>3</sup>Institute of Digital Materials Science (IDM), Karlsruhe University of Applied Sciences, Moltkestraße 30, 76133 Karlsruhe, Germany

<sup>a)</sup>Author to whom correspondence should be addressed: [fei.wang@kit.edu](mailto:fei.wang@kit.edu)

## ABSTRACT

Variations from equilibrium Young's angle, known as contact angle hysteresis (CAH), are frequently observed upon droplet deposition on a solid surface. This ubiquitous phenomenon indicates the presence of multiple local surface energy minima for the sessile droplet. Previous research primarily explains CAH via considering macroscopic roughness, such as topographical defects, which alter the effective interfacial energy between the fluid phase and the solid phase, thereby shifting the global surface energy minimum. One typical example is the classic Cassie–Baxter–Wenzel theory. Here, we propose an alternative microscopic mechanism that emphasizes the complexity of molecular rearrangements at the fluid–solid interface, treating their interfacial tensions as variables, which results in multiple local surface energy minima. Our theoretical framework demonstrates that CAH can occur even on chemically homogeneous and mechanically smooth-flat substrates, aligning with previously unexplained experimental observations. In addition, we explore the interplay between macroscopic and microscopic roughness in influencing CAH and clarify the contrasting wetting behaviors—the lotus effect and the rose petal effect—on hierarchical roughness from a thermodynamic perspective. This work provides valuable insights into surface tension determination by restoring the natural physical properties of interfaces and illuminates the multifaceted mechanisms underlying the everyday occurrences of CAH.

© 2024 Author(s). All article content, except where otherwise noted, is licensed under a Creative Commons Attribution-NonCommercial 4.0 International (CC BY-NC) license (<https://creativecommons.org/licenses/by-nc/4.0/>). <https://doi.org/10.1063/5.0232287>

## I. INTRODUCTION

When a droplet is placed on a substrate, a contact angle  $\theta$  [see Fig. 1(a)] is formed at the triple junction of the droplet-gas-substrate system. This wetting phenomenon was first fully described by classical Young's law<sup>1</sup> in the early 1800s, with its validity confirmed in recent decades through both numerical<sup>2,3</sup> and analytical<sup>4,5</sup> methods. In the analytical method, the free energy minimization approach is often applied, with interfacial tensions considered as inherent material properties and constants. Consequently, the system surface energy  $E$  is solely a function of the contact angle  $\theta$  with a global minimum (see Sec. II for the explicit derivations), yielding a unique equilibrium Young's angle (denoted as  $\theta_e$ ) on chemically homogeneous and mechanically smooth-flat

substrates. This relationship is expressed mathematically as

$$\cos \theta_e = \frac{\gamma_{sg} - \gamma_{sl}}{\gamma_{lg}}, \quad (1)$$

where  $\gamma_{sg}$ ,  $\gamma_{sl}$ , and  $\gamma_{lg}$  are the interfacial tensions of the solid–gas, solid–liquid, and liquid–gas phases, respectively. While the validity of Young's law is undisputed, it assumes ideal conditions, ignoring substrate imperfections and intermolecular interactions at the contact surface, which are rarely encountered in real life. Thus, classical Young's law with single energy minimum fails to explain the mechanism behind the critical phenomenon: contact angle hysteresis (CAH).

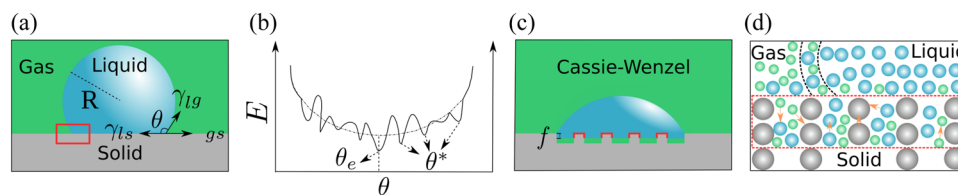


**FIG. 1.** Contact angle hysteresis (CAH). (a) Sessile droplet with cap radius  $R$  and contact angle  $\theta$  on a solid substrate. The interfacial tensions at liquid–gas, solid–liquid, and solid–gas interfaces are denoted as  $\gamma_{lg}$ ,  $\gamma_{sl}$ , and  $\gamma_{sg}$ , respectively. (b) Multiple local minima in the free energy of the droplet–gas–substrate system result in various metastable contact angles  $\theta^*$  and contribute to CAH.  $\theta_e$  corresponds to the global minimum of  $E$ . Reproduced with permission from Butt *et al.*, *Curr. Opin. Colloid Interface Sci.* **59**, 101574 (2022). Copyright 2022, Elsevier. (c) Macroscopic roughness on the solid substrate induces CAH in the Cassie–Wenzel state. Parameter  $f$  indicates the extent of wetting transition between Cassie–Baxter and Wenzel states with fully wet  $f = 1$ . (d) Microscopic roughness induced by molecular rearrangements contributes to CAH. Blue, green, and gray dots represent liquid, gas, and solid molecules, respectively. The red dashed line encloses the fluid–solid interfacial region, with arrows indicating intermolecular interactions. The black dashed line outlines the liquid–gas interface.

Here, CAH refers to the phenomenon where a droplet forms different contact angles with a given substrate. This phenomenon has been observed in both nature and industry, impacting the self-cleaning ability of lotus leaves, waterproof nature of butterfly wings, high-resolution inkjet printing, and drug delivery in pharmaceuticals. Understanding the mechanisms behind CAH offers insights into both fundamental physics and practical technologies. In physics, it assists in measuring interfacial tensions,<sup>6</sup> studying soft surfaces with folding memory,<sup>7</sup> and investigating pinning-depinning dynamics of moving contact lines.<sup>8</sup> Technologically, understanding CAH can optimize energy storage efficiency,<sup>9</sup> control functional surface properties,<sup>10</sup> and improve circuit printing quality,<sup>11,12</sup> among other applications.

Recent research<sup>13</sup> suggests that CAH arises from substrate imperfections, leading to a non-monotonic energy landscape of the droplet system. Figure 1(b) illustrates CAH, showing several metastable contact angles ( $\theta^*$ ), each representing a local minimum of  $E$  that deviates from the global minimum with equilibrium Young's angle  $\theta_e$ . This indicates that CAH, characterized by multiple metastable states, is linked to substrate roughness. In this work, we examine substrate roughness at two length scales: microscopic and macroscopic.

Real solid surfaces are rarely free of macroscopic roughness. Consequently, CAH has been primarily attributed to macroscopic roughness, including the chemical or morphological heterogeneity of the substrate.<sup>14,15</sup> Given our focus on microscopic roughness, this work specifically addresses the morphological imperfections associated with macroscopic roughness. Figure 1(c) depicts the typical Cassie–Wenzel state, where the impregnation factor  $f$  represents the degree of wetting transition with complete wetting  $f = 1$ . Introducing this morphological roughness into Young's law alters the real contact area and thus the effective interfacial energy beneath the droplet,<sup>5,16</sup> shifting  $\theta_e$  for certain  $f$ . This mechanism is well described by the Cassie–Wenzel equations,<sup>17</sup> which help to heed CAH.

Alternatively, experimental evidence indicates that CAH can also occur even on microscopically smooth and chemically homogeneous substrates.<sup>18–20</sup> This phenomenon is attributed to molecular rearrangements at the solid–liquid and solid–gas interfaces upon droplet placement.<sup>21–23</sup> Researchers<sup>18–23</sup> suggest that CAH on smooth surfaces reflects the intrinsic properties of intermolecular interactions at the fluid–solid interfaces. To scrutinize CAH

in these cases, we define these molecular rearrangements as microscopic roughness, following the framework proposed by Wang *et al.*<sup>24</sup> At the molecular level, microscopic roughness emanates from several microstructural inhomogeneities, such as polar groups, chain lengths, molecular volume, liquid molecule orientation,<sup>25</sup> and surface composition.<sup>26,27</sup> Figure 1(d) zooms in on the triple-line interface region highlighted by the red dashed box.

The mechanism of CAH due to macroscopic roughness is rather well established through the Cassie–Wenzel equations, whereas the mechanism at the microscopic roughness level remains unclear due to the complexities associated with nanometer and molecular scales near the contact line. The structures and dynamics among liquid, gas, and solid molecules in this narrow region are largely unexplored and remain a significant challenge. For instance, these complex intermolecular interactions can alter the surface composition, thereby changing the interfacial tensions.<sup>28</sup> The interfacial tensions are expected to vary with surface composition.<sup>29,30</sup> Based on this assumption, the classical Young's law becomes invalid. To clarify this CAH phenomenon, Bormashenko<sup>31</sup> suggests augmenting the system surface energy  $E$  with additional 1D energy, such as the heat release at the triple line or line tension, although the validity of line tension concept remains open to discussion.<sup>32–35</sup> Starov *et al.*<sup>36,37</sup> approach the issue by considering the contribution of Derjaguin's pressure around the adsorption film to the excess free energy, effectively elucidating CAH on smooth-flat substrates. However, this model's applicability is constrained by the presence of the adsorption layer.<sup>38–42</sup> Therefore, a comprehensive mechanism explaining the role of microscopic roughness in CAH remains to be developed.

The overarching challenge in understanding the influence of microscopic roughness on CAH stems from the wide range of length scales involved, from millimeter-sized droplets to nanoscale structures near the contact line. Although the fluid–solid interface appears relatively sharp compared to droplet dimensions, at the microscopic scale, the molecular arrangement at the fluid–solid interface is neither perfectly ordered nor confined to a strictly two-dimensional boundary.<sup>43</sup> Instead, the fluid–solid interface forms a finite region where molecules from the solid and adjacent fluid phases coexist. Their intermolecular interactions give rise to variable interfacial tensions between the fluid phases and the solid surface. As proposed in Ref. 44, it is reasonable to consider the contribution of mobile components within the fluid–solid interfacial region to the

interfacial tensions, which play a critical role in CAH. In line with this concept, we treat the solid–gas and solid–liquid interface as a finite volume region, where short-range van der Waals forces act on the gas, liquid, and solid molecules. To capture these intermolecular interactions, we introduce the concept of wall energy density, denoted as  $\Gamma$ , to represent the variable fluid–solid interfacial tensions. We assume that the wall energy density is a function of the substrate’s surface composition of liquid molecules, similar to the Gibbs adsorption isotherm, where surface tension varies with surface composition. Unlike the traditional definition of solid–liquid and solid–gas interfacial tensions in Young’s law, where their difference is typically inferred from contact angle measurements and difficult to investigate separately, the introduction of wall energy density provides a clearer framework. This concept allows for incorporating distinct intermolecular forces that independently affect solid–liquid and solid–gas interfacial tensions. By systematically analyzing the influence of wall energy density on CAH, we can replicate the complexity of fluid–solid interfacial tensions ( $\gamma_{sg}$ ,  $\gamma_{sl}$ ) as observed in the physical world. It is worth noting that in reality, fluid–solid interfacial tensions are influenced by several factors, including, but not limited to, surface composition, chemical changes (e.g., hydrogen bonding and electrostatic interactions), and environmental conditions (e.g., temperature and pressure). Here, we first consider the case where interfacial tensions are affected by surface composition. More complex cases will be discussed in Sec. III B. Upon introducing  $\Gamma$  into Young’s law, the complex intermolecular manner in the interface region is coupled with Young’s law. This approach reveals the significance of microscopic roughness in CAH, demonstrating it on mechanically smooth-flat and chemically homogeneous substrates.

Utilizing the energy minimization method, we propose a general CAH mechanism that incorporates both microscopic and macroscopic roughness. By combining these roughnesses across different scales, we elucidate the fundamental thermodynamic mechanisms behind the contrasting behaviors of CAH: the lotus effect, characterized by high contact angles with small CAH, and the rose petal effect,<sup>45</sup> featuring high contact angles with significant CAH. This mechanism can be harnessed and extended by exploring the physical implications of wall energy density in more intricate wetting scenarios. This study sheds light on the multifaceted mechanisms underlying CAH, enriching our understanding of the phenomenon’s complexity and is crucial for advancing future microfluidics experiments.

## II. THEORETICAL METHODS

### A. Microscopic roughness model

In our study, the overall system free energy is described by the surface energy as

$$E = \gamma_{lg}A_{lg} + (\gamma_{sl} - \gamma_{sg})\pi(R \sin \theta)^2 + E_0, \quad (2)$$

with a constant reference state  $E_0 = \gamma_{sg}S_0$ , where  $S_0$  indicates the substrate surface area. The variables  $R$  and  $\theta$  are the droplet radius and the contact angle, respectively, as illustrated in Fig. 1(a).  $A_{lg}$  is the surface area of the liquid cap. It is worth noting that the apparent contact angle is not influenced by bulk energy and is solely constituted by the 2D and 1D energy contributions (for a detailed

derivation, see Ref. 31); the system energy here only considers the contribution of surface energy.

For a droplet with a given volume deposited on a mechanically smooth-flat and chemically homogeneous substrate with an apparent contact angle  $\theta$ , the volume  $V$  and  $A_{lg}$  are subjected to the following geometric constraints:

$$V = \frac{\pi}{3}R^3(2 + \cos \theta)(1 - \cos \theta)^2, \quad (3)$$

and

$$A_{lg} = 2\pi R^2(1 - \cos \theta). \quad (4)$$

By substituting Eqs. (3) and (4) into Eq. (2), the system surface energy is expressed as

$$E = \left[ \frac{9\pi V^2}{(2 + \cos \theta)^2(1 - \cos \theta)} \right]^{\frac{1}{3}} [2\gamma_{lg} + (\gamma_{sl} - \gamma_{sg})(1 + \cos \theta)]. \quad (5)$$

Whyman *et al.*<sup>5</sup> assume that the interfacial tensions in Eq. (5) are constants. Consequently, the system energy  $E$  in Eq. (5) solely depends on the contact angle  $\theta$ . The contact angle at the equilibrium state requires the global minimum of the entire system energy, namely,  $dE/d\theta = 0$ . This condition can be fulfilled when the equilibrium contact angle  $\theta_e$  is either  $0^\circ$  or  $180^\circ$ , or satisfies the relationship described in Eq. (1). The former corresponds to complete wetting/dewetting, while the latter signifies Young’s law. Excluding the energy extremum for complete wetting/dewetting, only one global energy minimum with a unique value of  $\theta_e$  exists in the framework of Young’s consideration.<sup>1</sup>

As mentioned in Sec. I, certain experiments<sup>20,21,23</sup> reveal that even on mechanically smooth-flat and chemically homogeneous substrates, CAH appears. In this context, the traditional Young’s law loses its validity. If we consider that the fluid–solid interfacial tensions  $\gamma_{sg}$  and  $\gamma_{sl}$  are no longer constant, the above derivation for Young’s law<sup>1,5</sup> needs further improvement.

As the assumption in Ref. 46, the interfacial tension between liquid and gas phases remains constant, while the fluid–solid interfacial tensions may vary with the wetting processes. This implies that treating the interfacial tensions  $\gamma_{sl}$  and  $\gamma_{sg}$  as constants in classical Young’s law is a simplification. To address this, we introduce the wall energy density,  $\Gamma$ , to represent the variable fluid–solid interfacial tensions. Aligned with the concept proposed by Cahn *et al.*,<sup>47,48</sup> wall energy density can vary with the surface composition of fluids on the substrate. This variation arises from the wall effect,<sup>29</sup> where the fluid composition near the substrate deviates from that in the bulk phases when fluids partially penetrate into the solid wall. Wang *et al.*<sup>24</sup> further express wall energy density as a function of the average volume fractions of liquid molecules, whether they belong to the liquid or gas phase, in the fluid–solid interfacial region. Following this approach, the variable fluid–solid interfacial tensions ( $\gamma_{sl}$  and  $\gamma_{sg}$ ) at the substrate are expressed as

$$\gamma_{sl} = \Gamma(\phi_l); \quad \gamma_{sg} = \Gamma(\phi_g), \quad (6)$$

where  $\phi_l$  and  $\phi_g$  represent the average volume fractions of liquid molecules in the liquid and gas phases near the solid surface, respectively. These variables are independent, with  $\phi_l \in [0, 1]$  and

$\phi_g \in [0, 1]$ . Their equilibrium values of  $\phi_l$  and  $\phi_g$  are determined through energy minimization [detailed derivations provided later in Eqs. (10)–(14)]. At equilibrium, the corresponding wall energy density values represent the experimentally measured solid–liquid and solid–gas interfacial tensions.

Landau and Lifshitz<sup>46</sup> suggest that any formulation of interfacial tensions  $\gamma_{sg}$  or  $\gamma_{sl}$  is appreciated during the wetting process. Moreover, a polynomial approach aligns well with the concept of subregular solution model.<sup>49,50</sup> In this work, we express the wall energy density as a polynomial of the surface composition  $\phi$  as

$$\Gamma(\phi) = a + b\phi + c\phi^2 + d\phi^3 + \dots, \quad (7)$$

where  $\phi$  signifies either  $\phi_l$  or  $\phi_g$ . The coefficients  $a, b, c, d$  characterize the intermolecular attraction and repulsion at the interface between the solid wall and adjacent fluid phases, as described by De Gennes in Ref. 51. Unlike the parabolic form used by Wang *et al.*,<sup>24</sup> we here introduce higher-order terms in Eq. (7) to more accurately capture the unidealized solution behaviors through van der Waals forces within the fluid–solid interfacial region, reflecting the complexity of interactions among liquid, gas, and solid molecules. Given that the variable interfacial tensions in Eq. (6) are assumed to depend solely on the liquid molecular composition, the coefficients in Eq. (7) for both fluid–solid interfacial tensions should therefore have identical values. These parameters are influenced by various factors, including but not limited to material properties such as the polar groups of molecules and environmental conditions like temperature. The subsequent Sec. III B will provide detailed discussions on the physical significance of the wall energy density parameters.

By substituting the variable fluid–solid interfacial tensions from Eq. (6) into Eq. (5), the system energy is rewritten as

$$E = \left[ \frac{9\pi V^2}{(2 + \cos \theta)^2 (1 - \cos \theta)} \right]^{\frac{1}{3}} \times \{2\gamma_{lg} + [\Gamma(\phi_l) - \Gamma(\phi_g)](1 + \cos \theta)\}. \quad (8)$$

Now the system surface energy  $E$  in Eq. (8) becomes a multidimensional functional with respect to variables  $\theta$ ,  $\Gamma(\phi_l)$ , and  $\Gamma(\phi_g)$ . To identify the local minima and corresponding equilibrium states of  $E$ , a necessary equilibrium requirement is  $\partial E / \partial \theta = 0$ . Apart from the cases of complete wetting/dewetting, this condition can lead to Young's law as well:

$$\cos \Theta = \frac{\Gamma(\phi_g) - \Gamma(\phi_l)}{\gamma_{lg}}. \quad (9)$$

Here,  $\Theta[\Gamma(\phi_g), \Gamma(\phi_l)]$ , unlike the unique value  $\theta_e$  in Eq. (1), is a function of the variable fluid–solid interfacial tensions  $\Gamma(\phi_l)$  and  $\Gamma(\phi_g)$ . It denotes the specified contact angles that satisfy the partial derivatives constraint in the  $\theta$  space. However, it is important to note that the condition  $\partial E / \partial \theta = 0$  alone is insufficient to determine the local minima of  $E$ ; it is also necessary to account for the local minima in the space of interfacial tensions. At equilibrium, the feasible metastable states  $\theta^*$  in  $\Theta$  space can be obtained by further determining the minimum of  $E$  in Eq. (8) in the  $\Gamma(\phi_g)$  and  $\Gamma(\phi_l)$  spaces simultaneously.

By substituting Eq. (9) into Eq. (8), we express the entire system surface energy in terms of the independent variables  $\phi_g$  and  $\phi_l$ :

$$E = (9\pi V^2)^{\frac{1}{3}} \gamma_{lg} \left[ 2 + \frac{\Gamma(\phi_g) - \Gamma(\phi_l)}{\gamma_{lg}} \right]^{\frac{1}{3}} \left[ 1 - \frac{\Gamma(\phi_g) - \Gamma(\phi_l)}{\gamma_{lg}} \right]^{\frac{2}{3}}. \quad (10)$$

The liquid–gas interfacial tension  $\gamma_{lg}$  is treated as a constant, following the concept of Landau and Lifshitz.<sup>46</sup> Now, the equilibrium or metastable state of the droplet necessitates a local minimum of  $E[\Gamma(\phi_g), \Gamma(\phi_l)]$  in Eq. (10) within the function domain  $\Omega = \{(\phi_g, \phi_l) | 0 \leq \phi_g \leq 1, 0 \leq \phi_l \leq 1\}$ . Two partial derivatives are given by

$$\frac{\partial E}{\partial \phi_g} = -\gamma_{lg} (9\pi V^2)^{\frac{1}{3}} \frac{\partial \Gamma(\phi_g)}{\partial \phi_g} \frac{A^{-\frac{2}{3}} B^{\frac{2}{3}} - 2A^{\frac{1}{3}} B^{-\frac{1}{3}}}{3}, \quad (11)$$

and

$$\frac{\partial E}{\partial \phi_l} = \gamma_{lg} (9\pi V^2)^{\frac{1}{3}} \frac{\partial \Gamma(\phi_l)}{\partial \phi_l} \frac{A^{-\frac{2}{3}} B^{\frac{2}{3}} - 2A^{\frac{1}{3}} B^{-\frac{1}{3}}}{3}, \quad (12)$$

with  $A = 2\gamma_{lg} + \Gamma(\phi_g) - \Gamma(\phi_l)$  and  $B = \gamma_{lg} - \Gamma(\phi_g) + \Gamma(\phi_l)$ , respectively. To find the minimum of  $E[\Gamma(\phi_g), \Gamma(\phi_l)]$  for the entire system, we analyze the stationary values  $\Phi_g^*$  and  $\Phi_l^*$  by setting Eqs. (11) and (12) to zero and examine the boundary conditions with 0 and 1.

The last part in Eqs. (11) and (12) fulfills  $\frac{1}{3}A^{-\frac{2}{3}}B^{\frac{2}{3}} - \frac{2}{3}A^{\frac{1}{3}}B^{-\frac{1}{3}} \leq 0$ .  $\frac{1}{3}A^{-\frac{2}{3}}B^{\frac{2}{3}} - \frac{2}{3}A^{\frac{1}{3}}B^{-\frac{1}{3}} = 0$  indicates a critical wetting case with  $\cos \theta = -1$ , that is, the contact angle of the droplet equals  $180^\circ$  on a super-hydrophobic substrate, which is beyond our discussion. Thus, for partial wetting,  $\partial E / \partial \phi_g = \partial E / \partial \phi_l = 0$  simplifies to

$$\frac{\partial \Gamma(\phi_g)}{\partial \phi_g} = 0, \quad \frac{\partial \Gamma(\phi_l)}{\partial \phi_l} = 0. \quad (13)$$

We denote

$$\Phi_g \in \{\Phi_g^*, 0, 1\}, \quad \Phi_l \in \{\Phi_l^*, 0, 1\}. \quad (14)$$

Consequently,  $E(\Phi_g, \Phi_l)$  represents the stationary value for the system surface energy. Further discussion on the possibility of a local minimum is conducted with the assistance of the energy landscape. By substituting the value defined at the local minimum of  $E$  from Eq. (14) into Eq. (9), the metastable contact angle can be subsequently determined.

## B. Combined roughness model

Taking substrate morphology into account, the system surface energy should be reformulated to incorporate both macroscopic (e.g., through Cassie–Wenzel equations) and microscopic roughness simultaneously. Here, we focus on discussing the influence of the substrate's complex morphology on the CAH phenomenon. To simplify, we consider the droplet to be sufficiently large in comparison with the scale of macroscopic roughness (detailed scale-dependent considerations can be found in the work of Michael and Bhushan<sup>54</sup>). This assumption implies two key points: first, the gas–liquid interface between two asperities can be treated as planar, that is, the curvature effect in this region can be neglected; second, the volume of liquid phase immersed in grooves is negligible. Moreover,

hierarchical (multiscale) roughness is ubiquitous in nature, as seen on the surfaces of lotus leaves,<sup>55</sup> rose petals,<sup>45</sup> and Salvinia leaves.<sup>53</sup> While all of these surfaces exhibit high hydrophobicity, their multiscale roughness results in distinct wetting behaviors. For instance, both the rose petal and lotus leaves feature high contact angles; however, the rose petal effect is characterized by significant CAH and strong water adhesion, while the lotus effect displays slight CAH and low adhesion to the substrate.

To illustrate how complex substrate morphology introduces multiple local minima in system surface energy  $E$ , and subsequently affects contact angles and CAH, we present three distinct instances that mimic typical natural macroscopic roughness, characterized by the presence of hierarchical structures. The SEM micrographs in Figs. 2(a-1)–2(c-1) show detailed morphological micro- and nanostructures of the surfaces: a lotus replica without hierarchical structures (first-level roughness), a Salvinia leaf with non-spherical roughness (i.e., combined head and tail structures), and a lotus leaf with complicated hierarchical structures (second-level roughness), respectively. These SEM images are reproduced from the works of Koch *et al.*<sup>52</sup> and Gandyra *et al.*<sup>53</sup> The subplots in Figs. 2(a-2)–2(c-2) illustrate the two-dimensional surface profiles of these instances: semicircle (I), bottle-shaped (II), and tree-shaped (III), respectively.

After introducing these multiscale roughnesses on the substrate, we define two parameters,  $\omega$  and  $r_\omega$ , to describe the effective contact area between solid–liquid–gas phases under the droplet. Specifically,  $\omega$  represents the fraction of the projected area of the wet solid surface, while  $1 - \omega$  indicates the fraction of the liquid–gas interface beneath the droplet. The parameter  $r_\omega$  describes the roughness factor of the wet area. Thus, the product  $\omega \cdot r_\omega$  quantifies the solid–liquid interface area per unit area. For simplicity, we consider two-dimensional profiles and use the arc length per unit length of the wet area as the roughness  $\omega \cdot r_\omega$ , instead of integrating over the entire bulk surface area. This simplification is justified by the axisymmetric nature of the bulk structure, which ensures a direct correlation between the extremum changes in the two-dimensional arc length and the wet area. However, these two parameters alone are insufficient to fully characterize the hierarchical variations in the substrate’s morphological roughness. To address this, we introduce the impregnation factor,  $f$ , to capture the degree of wetting

transition between Cassie–Baxter and Wenzel states, with  $f \in [0, 1]$ . Consequently, these parameters are defined as

$$\omega = \frac{l_p}{l_a}, \quad r_\omega = \frac{l_s}{l_p}, \quad f = \frac{h}{H}, \quad (15)$$

where  $l_p$ ,  $l_a$ ,  $l_s$ ,  $h$ , and  $H$  represent the half length of the wet arc projection, half periodicity between two asperities, half arc length of the wet surface, height of the wet surface, and height of the asperities, respectively, as illustrated in Figs. 2(a-2)–2(c-2). The solid red line in the figure denotes the wet solid surface.

For clarity, we here nondimensionalize both the wet arc projection half-length  $l_p$  and the half periodicity length  $l_a$  using their respective characteristic lengths. This allows  $l_p$  to be expressed as a function of the impregnation factor  $f$ , rather than directly depending on the height of the wet surface  $h$ . In this framework, we assume that the ratio of asperity height  $H$  to the half periodicity length  $l_a$  is equal to 1, similar to the method used in boundary layer theory in fluid mechanics. As a result, both  $\omega$  and  $r_\omega$  are the functions of the impregnation factor,  $f$ , and depend on the specific substrate morphology. For the respective instances, the expressions for  $\omega$  and  $f$ , as well as for the roughness ratio  $r_\omega$  and  $f$ , are as follows:

$$\text{I: } \omega = \sqrt{2f - f^2}, \quad \omega \cdot r_\omega = \arcsin \omega(f), \quad (16)$$

$$\text{II: } \omega = 9.67f^3 - 13.08f^2 + 4.31f + 0.1, \quad \omega \cdot r_\omega = \omega(0) + \int_0^f \sqrt{1 + [\omega'(f)]^2} df, \quad (17)$$

$$\text{III: } \omega = \left\{ (f + 1) \left[ \left( \sin \frac{3\pi}{2} f \right)^2 - 0.5 \right] \right\}^2, \quad \omega \cdot r_\omega = \omega(0) + \int_0^f \sqrt{1 + [\omega'(f)]^2} df. \quad (18)$$

It is worth noting that, in this framework, we limit the ratio  $H/l_a$  to 1 and do not explore how the spatial constraints affect CAH. This limitation can be easily investigated in future work by directly

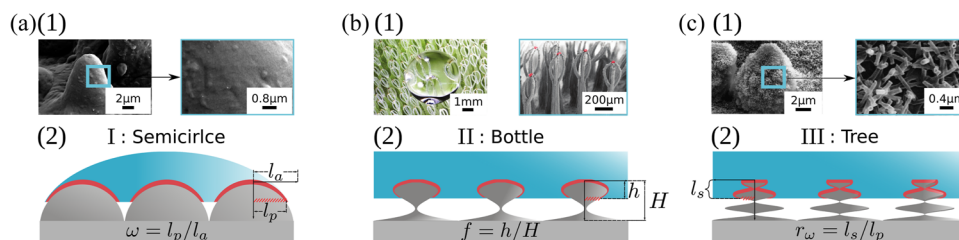


**FIG. 2.** Schematics of macroscopic roughness SEM images in the top panel showcase three distinct surfaces in nature: lotus replica with first-level roughness, Salvinia leaf with non-spherical roughness, and lotus leaf with second-level roughness. (a)(1) and (c)(1) Reproduced from Koch *et al.*, *Soft Matter* 5, 1386 (2009) with permission from the Royal Society of Chemistry. (b)(1) Reproduced from Gandyra *et al.*, *Small* 16, 2003425 (2020). Copyright 2020 Author(s), licensed under a Creative Commons Attribution License. The bottom panel corresponds to macroscopic roughness schematics (dark gray). The solid red line indicates the wetting solid surface.  $l_p$ ,  $l_a$ ,  $h$ ,  $H$ , and  $l_s$  represent the half length of the wet arc projection (i.e., the hatched area), half periodicity between two asperities, height of the wet surface, height of the asperities, and half arc length of the wet surface, respectively.  $\omega$  represents the fraction of the projected area of the wet solid surface. The impregnation factor  $f$  captures the degree of wetting transition between Cassie–Baxter and Wenzel states.  $r_\omega$  describes the roughness factor of the wet area.

incorporating the actual physical lengths of  $l_p$  and  $l_a$  into  $\omega$ , based on specific substrate morphology. Consequently,  $E$  is given by

$$E = \gamma_{lg}A_{lg} + \{ [\Gamma(\phi_l) - \Gamma(\phi_g)] [\omega(f) \cdot r_\omega(f)] + \gamma_{lg}[1 - \omega(f)] \} \pi(R \sin \theta)^2 + E_0. \quad (19)$$

The second term on the right-hand side incorporates both the microscopic and macroscopic roughness, contributing to the effective interfacial energy beneath the droplet.

### III. RESULTS AND DISCUSSION

#### A. Microscopic roughness

In this section, we first demonstrate the microscopic roughness-induced CAH phenomenon on mechanically smooth-flat and chemically homogeneous substrates by applying the surface composition-dependent wall energy density concept to Young's law.<sup>24</sup> The limitations inherent in Young's<sup>1</sup> simplistic treatment of interfacial tensions as constants are discussed. Utilizing the energy landscape method, subsequent paragraphs examine the impact of various wall energy density formulations on CAH. Moreover, the complexity of multiple local energy minima hidden behind in Fig. 1(b) is clarified to mitigate potential misunderstandings.

In Fig. 3(a-1), the linear wall energy density function with  $\Gamma(\phi) = a + b\phi$  is plotted, which is normalized here for clarity. Here, we denote  $\theta^*$  as the metastable contact angle corresponding to each energy minimum. When multiple metastable contact angles exist,  $\theta^*$  is indexed as  $\theta_i^*$ , where  $i \in \mathbb{Z}^+$ , as indicated by the colored dots in Fig. 3. By setting  $b = 0$ , the wall energy density  $\Gamma$  becomes independent of composition, leading to a constant system energy  $E$  in Eq. (10). This returns to the classical Young's law consideration with constant fluid–solid interfacial tensions. Substituting this constant wall energy density into Eq. (9) yields  $\cos \theta^* = 0$ , corresponding to a consistent  $90^\circ$  contact angle. For non-zero  $b$ , setting  $a = 0.5$  and  $b = 0.8$  in the wall energy density  $\Gamma(\phi)$  and substituting it into  $E$  [see Eq. (10)], the energy landscape of system surface energy is illustrated in Fig. 3(a-2). A single energy minimum with  $\phi_g = 1$  and  $\phi_l = 0$  appears at the upper-left corner of the droplet energy landscape for  $b > 0$  (for  $b < 0$ , the energy minimum is at the lower-right with  $\phi_g = 0$  and  $\phi_l = 1$ , see supplementary material). Only one stable contact angle corresponds to the unique energy minimum, denoted as  $\theta_1^*$ . By substituting the boundary values of  $\Omega = \{(\phi_g, \phi_l) | 0 \leq \phi_g \leq 1, 0 \leq \phi_l \leq 1\}$  into Eq. (9), the only equilibrium contact angle is expressed as  $\theta_1^* = \arccos|b|$ , indicating that no CAH exists for the linear relationship of  $\Gamma$  with  $\phi$ . Within this framework, the formulation exclusively characterizes the hydrophilic wetting condition with  $\cos \theta_1^* \geq 0$ . The hydrophobic setup can

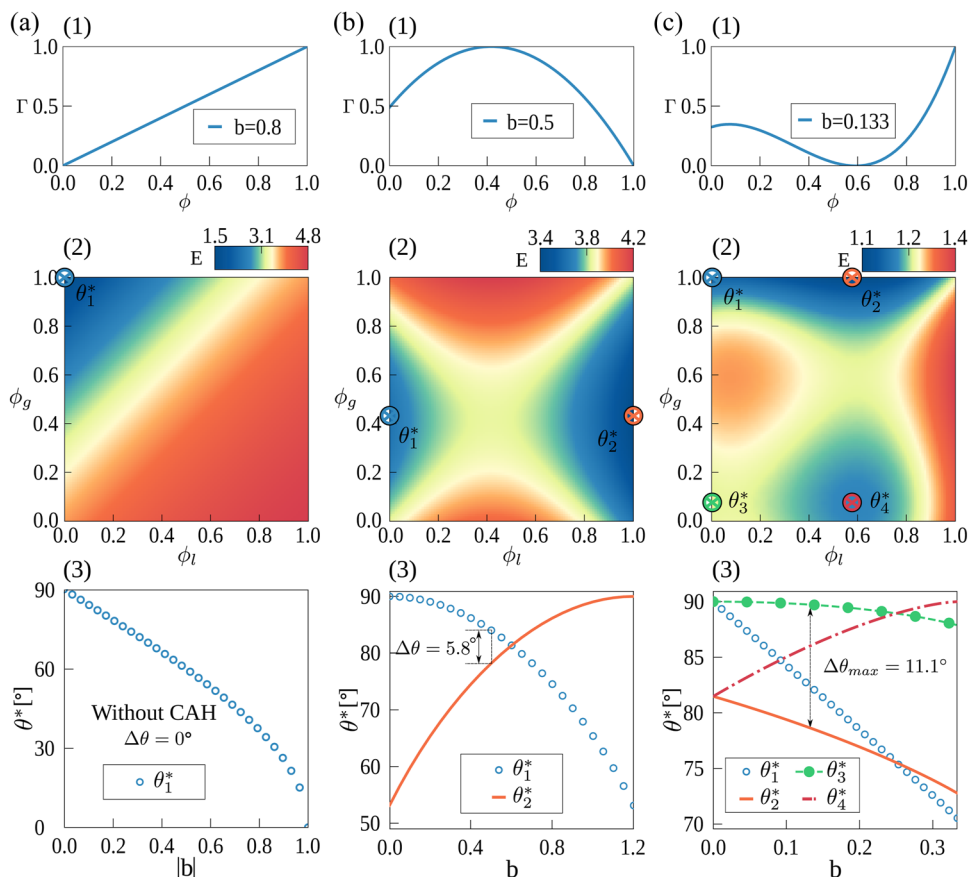


**FIG. 3.** Effects of microscopic roughness-induced CAH. The top, middle, and bottom panels represent wall energy density functions  $\Gamma(\phi)$ , system total surface energy landscape  $E[\Gamma(\phi_g), \Gamma(\phi_l)]$  [see Eq. (10)], and metastable contact angles  $\theta_i^*$ , respectively. (a) No CAH observed. (1) Linear  $\Gamma(\phi)$  without a stationary point in the function domain  $\Omega$ . (2) Singular energy minimum with  $\phi_g = 1$ ,  $\phi_l = 0$  on the energy landscape indicates a unique stable contact angle  $\theta_1^*$ . (3) Changes in the wall energy density parameter  $|b|$  monotonically vary the stable contact angle  $\theta_1^*$ . (b) CAH with two metastable contact angles  $\theta_1^*$  and  $\theta_2^*$ . (1) Parabolic  $\Gamma(\phi)$  with one stationary point in  $\Omega$ . (2) Complex molecular interactions in the fluid–solid interface reflected by the complex  $\Gamma(\phi)$ , resulting in multiple energy extrema in  $E$ . (3) Manipulating parameter  $b$  to change  $\Gamma(\phi)$  alters the significance of CAH. (c) CAH with four  $\theta_i^*$ . (1) Cubic  $\Gamma(\phi)$  with two stationary points in  $\Omega$ . (2) Four energy minima and corresponding metastable contact angles. (3) The complexity of  $\Gamma(\phi)$  leads to more intricate CAH.

be obtained by replacing  $\theta_1^*$  with  $180^\circ - \theta_1^*$ . The value of  $\theta_1^*$ , initially observed as  $\theta_1^* = 36.9^\circ$  with  $b = 0.8$ , can be modified by varying the value of  $|b|$ . Notably, the outcomes for partial hydrophilic wetting using the linear formulation of wall energy density align with the original Young's law, where both cases treat interfacial tensions as a linear function of  $\phi$ , neglecting the complex multi-body molecular interactions in interface regions, and exhibit a singular global minimum.

Figure 3(b-1) depicts the parabolic wall energy density  $\Gamma(\phi) = a + b\phi + c\phi^2$  with a stationary point  $\Phi_1^*$  and  $\Phi_g^*$  in  $\Omega$ . Without loss of generality, we present one instance with parameters  $a = 0.5$ ,  $b = 0.5$ , and  $c = -0.6$  for hydrophilic wetting. The corresponding energy landscape, based on Eq. (10), is presented in Fig. 3(b-2). Different from Fig. 3(a-2), the presence of dual local minima at  $\phi_g = \Phi_g^*$ ,  $\phi_l = 0$  and  $\phi_g = \Phi_g^*$ ,  $\phi_l = 1$  is presented, indicating the existence of two metastable wetting states. This demonstrates the CAH phenomenon on a chemically homogeneous and smooth-flat substrate without introducing extra line tension or macroscopic roughness. The associated contact angles, corresponding to the dual local minima in the energy landscape, are denoted as  $\theta_1^*$  for  $E(\phi_g = \Phi_g^*, \phi_l = 0)$  and  $\theta_2^*$  for  $E(\phi_g = \Phi_g^*, \phi_l = 1)$ , as depicted in Fig. 3(b-2). Substituting the two local minimum points ( $\phi_g = \Phi_g^*, \phi_l = 0$ ) and ( $\phi_g = \Phi_g^*, \phi_l = 1$ ) into the model Eq. (9), the expressions of  $\theta_1^*$  and  $\theta_2^*$  in terms of parameters  $b$  and  $c$  of the parabolic  $\Gamma(\phi)$  are simplified as follows:

$$\cos \theta_1^* = -\frac{b^2}{4c}, \quad \cos \theta_2^* = -\frac{(b+2c)^2}{4c}. \quad (20)$$

When applying Eq. (20), it is essential to consider the specific criteria governing the range of values for both  $b$  and  $c$ . For instance, when fixing  $c$ , the range of  $b$  must adhere to two distinct conditions:

$$|\cos \theta_i^*| \leq 1; \quad 0 \leq \Phi_1^* \leq 1, \quad 0 \leq \Phi_g^* \leq 1. \quad (21)$$

The first criterion involves substituting  $b$  and  $c$  into Eq. (20) while ensuring that  $\cos \theta_i^* \in [-1, 1]$  (with  $i = 1, 2$ ), as the premise of all the above discussions is based on partial wetting in the current study. The second condition stipulates that there exists one stationary point in  $\Omega$  for the parabolic  $\Gamma(\phi)$ . Figure 2(b-3) illustrates the variation of the contact angles  $\theta_1^*$  and  $\theta_2^*$  as  $b$  varies within the range  $[0, 1.2]$ , with  $c$  fixed at  $-0.6$ . The contact angle hysteresis, denoted as  $\Delta\theta = \theta_1^* - \theta_2^*$ , is  $5.8^\circ$  at  $b = 0.5$ . By manipulating  $b$  in  $\Gamma(\phi)$  while keeping  $c = -0.6$ ,  $\Delta\theta$  is distributed over  $[0^\circ, 36.9^\circ]$ . This range can be further extended through fine-tuning parameters  $b$  and  $c$  within the parabolic wall energy density framework.

So far, a significant outcome of the present study is represented: utilizing the parabolic wall energy density function in  $E$  [see Eq. (10)] can quantitatively result in the existence of two metastable contact angles even on mechanically smooth-flat and chemically homogeneous substrates. The observed contact angle hysteresis is attributed to variations in solid-liquid and solid-gas interfacial tensions. These variations can be linked to diverse factors of microscopic roughness, such as surface compositions induced by various initial states due to deposition techniques,<sup>56</sup> and molecular rearrangements in the fluid-solid interfacial region upon droplet deposition. The molecular rearrangements can be controlled through material properties, temperature adjustments, and other factors. Precise control of CAH can be achieved by manipulating the wall energy density parameters.

Notably, experiments have revealed more complex scenarios for droplets under vibrations, where the "mean" contact angle follows  $\bar{\theta}^* = (\theta_1^* + \theta_2^*)/2$  or  $\cos \bar{\theta}^* = (\cos \theta_1^* + \cos \theta_2^*)/2$  in Refs. 57–59. Introducing such external vibrations can result in a droplet in a global energy minimum with a stable  $\theta_e$  as well. This suggests the existence of more than two metastable contact angles for such CAH phenomena. However, when applying the parabolic wall energy density, the maximum number of possible metastable contact angles is limited to two. To further explore the phenomenon of "mean" contact angle, a more intricate wall energy density formulation will be discussed in subsequent analyses. Our emphasis is on elucidating diverse metastable contact angles in the context of CAH, particularly those not explained by the parabolic wall energy density framework, as observed in vibration experiments. We begin by analyzing the most complex scenarios for the cubic  $\Gamma(\phi)$ , where there exist two stationary values within  $\Omega$ , exhibiting the most possible local minima for  $E$  [see Eq. (10)].

In Fig. 3(c-1), the cubic wall energy density formulation  $\Gamma(\phi) = a + b\phi + c\phi^2 + d\phi^3$  is plotted with two stationary values in  $\Omega$ . For clarity, the energy landscape of an instance with  $a = 0$ ,  $b = 0.1331$ ,  $c = -1$ , and  $d = 1$  is presented in Fig. 3(c-2). Consequently, multiple energy minima are observed, and the resulting contact angles are denoted as  $\theta_1^*$ ,  $\theta_2^*$ ,  $\theta_3^*$ , and  $\theta_4^*$ , respectively. Their expressions in terms of the coefficients in  $\Gamma(\phi)$  are

$$\begin{aligned} \cos \theta_1^* &= b + c + d, \\ \cos \theta_2^* &= \cos \theta_1^* + \frac{\cos \theta_4^*}{2} + \frac{9bcd - 2c^3}{27d^2}, \\ \cos \theta_3^* &= \frac{\cos \theta_4^*}{2} - \frac{9bcd - 2c^3}{27d^2}, \\ \cos \theta_4^* &= \frac{\Delta^3}{27d^2}, \end{aligned} \quad (22)$$

with  $\Delta = \sqrt{c^2 - 3bd}$ . Focusing on partial wetting cases, the parameters in the cubic  $\Gamma(\phi)$  must satisfy the following conditions:

$$|\cos \theta_i^*| \leq 1; \quad 0 \leq \Phi_{g_j}^* \leq 1, \quad 0 \leq \Phi_{l_j}^* \leq 1, \quad (23)$$

with  $j = 1, 2$ . The last condition ensures the existence of two stationary points in  $\Omega$  for the cubic  $\Gamma(\phi)$  and the presence of all listed metastable contact angles in Eq. (22). Figure 3(c-3) illustrates the various contact angle results when varying  $b$  within the range of  $[0, 1/3]$  while keeping ( $a = 0, c = -1, d = 1$ ) constant. The degree of CAH varies from  $0^\circ$  up to  $\sim 20^\circ$  as  $b$  changes. At  $b = 0.1331$ , the cosine values of contact angles satisfy  $\cos \theta_1^* = (\cos \theta_2^* + \cos \theta_4^*)/2$ , with the maximum CAH magnitude  $\Delta\theta_{\max} = 11.1^\circ$ . This range can be further extended by adjusting parameters in  $\Gamma(\phi)$ .

The number of  $\theta_i^*$  can be modified by adjusting the coefficients in the wall energy density, such as setting  $d = 0$  in the cubic  $\Gamma(\phi)$  to yield a single stationary value in  $\Omega$  and degenerate into the parabolic  $\Gamma(\phi)$ . Consequently, the discussed CAH phenomenon aligns with the parabolic  $\Gamma(\phi)$  (see supplementary material for this instance). The complexity of the extrema of wall energy density in  $\Omega$  determines the presence of multiple contact angle values for CAH (see the double-well example in supplementary material). A large number of studies<sup>60</sup> have shown that the expression of wall energy density is complex and remains unsolved, for instance, regarding

aqueous electrolytes where the wall energy density  $\Gamma$  is more appropriately expressed through Lennard-Jones potential or Coulomb potential.<sup>30,61</sup>

Real contact angles in the CAH phenomenon depend on various factors. This study demonstrates that when interfacial tensions are no longer considered as constants as classical Young's law assumes, CAH on a smooth-flat, chemically homogeneous substrate can be rigorously derived through the free energy minimization method with the concept of wall energy. The influences of different wall energy density formations on CAH, especially in complex scenarios with multiple metastable contact angles, are elucidated.

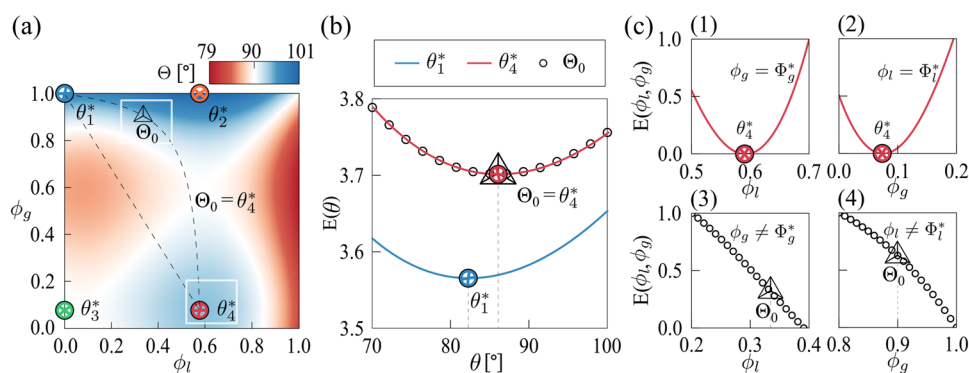
Here, we discuss the limitations of the conventional idea that the variation of  $E$  is exclusively determined by the apparent  $\theta$ , as outlined in  $E(\theta)$  in Sec. II, Eq. (5). Instead, we explore the intricate complexities involved in CAH, emphasizing the potential benefits of integrating the wall energy effect into  $E$ , expressed as  $E[\Gamma(\phi_g), \Gamma(\phi_l)]$  in Sec. II, see Eq. (10), and shedding light on its implications for future experimental investigations into interface tensions.

Figure 4(a) illustrates the landscape of  $\Theta$  from Eq. (9) using a cubic wall energy density relative to  $\phi_g$  and  $\phi_l$ , showcasing four metastable contact angles  $\theta_i^*$ , denoted with circles. These correspond to local energy minima [see Fig. 3(c-2)], with transitions requiring active energy to overcome energy barriers. Numerous contact angles identical to  $\theta_4^*$  emerge during transitions in the  $\Theta$  landscape. Dual dashed lines represent two possible transition pathways between  $\theta_1^*$  and  $\theta_4^*$ , with  $\Theta_0$  equaling  $\theta_4^*$ . Conventionally, the system surface energy is solely related to apparent  $\theta$ , that is,  $E(\theta)$  based on Eq. (5). Figure 4(b) depicts  $E(\theta)$  without considering variations in interfacial tensions, using specific constants derived from Fig. 4(a). An energy barrier separates metastable states  $\theta_1^*$  and  $\theta_4^*$ , both corresponding to energy minima. The energy functions  $E(\theta)$  of states  $\theta_4^*$  and  $\Theta_0$  overlap, both located at the minimum, yet the state  $\Theta_0$  is unstable, as depicted in Fig. 3(c-2). These observations indicate that the traditional model  $E(\theta)$  proves insufficient in explaining the CAH

phenomenon, as it typically maintains a singular energy minimum concerning  $\theta$ .

We further consider the influence of wall energy on  $E$ , extending the high dimensional space of  $\phi$  into  $E$ , that is,  $E[\Gamma(\phi_g), \Gamma(\phi_l)]$  derived from Eq. (10). Consequently,  $E$  becomes a high-dimensional functional with respect to  $\phi_g$  and  $\phi_l$ , where  $\theta$  is not an independent variable for obtaining the system's energy minimum and must be located in  $\Theta$  space, expressed with  $\phi_g$  and  $\phi_l$ . Figure 4(c) illustrates the energy function  $E[\Gamma(\phi_g), \Gamma(\phi_l)]$  of  $\theta_4^*$  and  $\Theta_0$ . While  $\theta_4^*$  reaches an energy minimum,  $\Theta_0$  does not. These results elucidate that the introduction of microscopic wall energy density impacts the wetting transition of a droplet from an initial contact angle  $\theta_1^*$  to a final angle  $\theta_4^*$ . Even though  $\Theta_0$  and  $\theta_4^*$  share the same value,  $\theta$  locating at  $\Theta_0$  does not mean the system reaching equilibrium. This is because, at the microscopic level, such a transition also requires molecular rearrangements, for example, through diffusion processes, to ensure  $\phi_g$  and  $\phi_l$  reach equilibrium in  $\phi$  space. These transitions induce variations in effective interfacial tensions  $\Gamma(\phi_g)$  and  $\Gamma(\phi_l)$  on a smooth-flat substrate. The interfacial tensions associated with  $\theta_4^*$  derived from Fig. 4(a) are favorable. These findings emphasize that achieving equilibrium in both microscopic  $\phi$  space and macroscopic  $\theta$  space is essential to attain the true energy extremum. This understanding underscores the necessity of considering the wall energy effect in future experimental investigations to accurately measure interfacial tensions associated with CAH.

Here, we establish the rationality of introducing wall energy density into the system surface energy, enhancing our understanding of the wetting transition between two metastable states of CAH. Our investigation reveals the inadequacy of the conventional  $E(\theta)$  model in explaining CAH, as it overlooks the influence of molecular interactions and fails to account for the high-dimensional nature of the system's surface energy landscape. By integrating the microscopic insights in  $\phi$  space alongside macroscopic  $\theta$  considerations, we achieve a more accurate depiction of the system energy  $E[\Gamma(\phi_g), \Gamma(\phi_l)]$ .



**FIG. 4.** Complexity behind CAH. (a) Contact angle  $\Theta$  with respect to different  $\phi_l$  and  $\phi_g$  by the cubic wall energy density function  $\Gamma(\phi)$ .  $\theta_i^*$  denotes the metastable contact angles corresponding to local surface energy minima. Dual dashed lines indicate the possible transition pathways from  $\theta_1^*$  to  $\theta_4^*$ . In one process, the value of  $\Theta_0$  (marked with dark triangle) equals  $\theta_4^*$ . (b) Without considering the microscopic roughness, the conventional formulation of total surface energy functions  $E(\theta)$  [Eq. (5)] for the metastable  $\theta_1^*$ ,  $\theta_4^*$ , and the unstable  $\Theta_0$ . An energy barrier exists between two metastable states  $\theta_1^*$  and  $\theta_4^*$ .  $\Theta_0$  lies also on the minimum of  $E(\theta)$ , but unstable due to the microscopic roughness mechanism. (c) Microscopic roughness considered, newly derived  $E[\Gamma(\phi_g), \Gamma(\phi_l)]$  by Eq. (10) with respect to the surface compositions  $\phi_g$  and  $\phi_l$ . The metastable  $\theta_4^*$  corresponds to an energy minimum, while the unstable  $\Theta_0$  does not. This complexity behind CAH highlights the microscopic roughness mechanism.

## B. Physical meaning discussion

So far, our visual demonstrations have shown that the CAH phenomenon on mechanically smooth-flat and chemically homogeneous substrates can be effectively elucidated by incorporating the notion of wall energy into classical Young's law. The influences of different wall energy density forms on CAH were discussed in detail. These discussions allow for a comprehensive understanding of the wetting process at a microscopic level. Here we discuss the rationality of the applied wall energy density formulation and the physical significance of its parameters.

Properly describing the molecular mechanism at the interface is crucial for deriving Young's law with CAH on a smooth-flat, chemically homogeneous substrate. According to Gibbs free energy, the interfacial tension of liquid/solid or gas/solid (denoted as wall energy density  $\Gamma$ ) is related to the internal energy and entropy, where the volume expansion in the interface is negligible. Therefore, the sub-regular solution model<sup>49,50</sup> can be applied to describe the van der Waals interactions within the fluid–solid interfacial region. This model is expressed as

$$\Gamma = \sum_{i < j} \chi_{ij} \phi^i \phi^j + \sum_i \chi_i \phi^i, \quad (24)$$

where  $\chi_{ij}$  and  $\chi_i$  represent the intermolecular potentials between the liquid and gas molecules and the fluid and solid molecules, respectively, as in the Flory–Huggins theory.<sup>62,63</sup> While following the concepts of Cahn and Landau,<sup>46,48</sup> any form  $\Gamma(\phi)$  is feasible and acceptable, as long as this form satisfies the following two assumptions: first, the interface between solid and liquid/gas phases is treated as continuum, and  $\phi$  varies smoothly across the interface; second, the interfacial tensions  $\Gamma(\phi)$  between solid and liquid/gas phases result from short-range interactions. De Gennes<sup>51</sup> reformulates Cahn's concept, expressing the wall energy density as a power series with respect to the liquid density at the substrate. The suitability of a power series is supported by two factors: first, any function can be infinitely approximated by a Taylor series; second, the power series aligns with the aforementioned sub-regular solution, with each coefficient possessing a corresponding physical meaning. More notably, writing  $\Gamma(\phi)$  in power series form is more general because the sub-regular model is more applicable to polymer systems.

The coefficients  $a$  and  $b$  in the power series of  $\Gamma(\phi)$  in Eq. (7) compound the influences of the internal energy  $\epsilon$ , Dalton's pressure (Landau's potential)  $\mathcal{P}$ , and van der Waals interaction  $\chi$ .  $\epsilon$  is exclusively influenced by temperature  $T$ .  $\mathcal{P}$  indicates the influence of external potential fields such as gravitational, electrostatic, and electromagnetic fields.  $\chi$  is influenced by the polar characteristics of the molecules involved. The parameters  $a$  and  $b$  are functions of  $(\epsilon, \mathcal{P}, \chi)$ , denoted as  $a(\epsilon, \mathcal{P}, \chi)$  and  $b(\epsilon, \mathcal{P}, \chi)$ . The parameter  $c$  or other higher order parameters denote an approximation to the nonlinear term  $\ln \phi$  introduced by grand potential in statistical mechanics view of Stirling approximation. Therefore, in practice, all these parameters in  $\Gamma(\phi)$  are determined by various complex factors such as temperature, gravity, and the polar group of molecules. A detailed discussion of these parameters in  $\Gamma(\phi)$  will help provide a better understanding of the daily phenomena in the wetting process. For instance, by constructing  $\Gamma(\phi)$  with the consideration of asymmetric densities between liquid/gas and solid phases, Wang *et al.*<sup>24</sup> successfully explained the counter-intuitive experiments<sup>64,65</sup>

showing that contact angle increases with temperature. In the future, additional effects, such as external potential fields (gravitational, electrostatic, and electromagnetic), temperature,<sup>66–68</sup> and time,<sup>69,70</sup> can be compounded into  $\Gamma(\phi)$  to discuss their influences on CAH, demonstrating the scalability of our model.

## C. Combined roughness

We further investigate the interplay between macroscopic and microscopic roughness in inducing CAH on rough substrates. By incorporating the macroscopic roughness characterized by the impregnation factor  $f$  into  $E$ , documented as  $E[f, \Gamma(\phi_g), \Gamma(\phi_l), \theta]$  in Eq. (19), we observe that, in alignment with the definition of  $\Gamma(\phi)$ , macroscopic roughness does not alter the stationary value  $\Phi^*$  and the local minima states of  $E$  in the  $\phi$  space. Utilizing the parabolic expression  $\Gamma(\phi)$  in  $E$ , extremes in the  $\phi$  space occur at either  $E(\phi_g = \Phi_g^*, \phi_l = 0)$  or  $E(\phi_g = \Phi_g^*, \phi_l = 1)$ . Thus, we can specify the values of interface tensions  $\Gamma(\phi_g)$  and  $\Gamma(\phi_l)$  as constants and denote their difference  $\Delta\Gamma = \Gamma(\phi_g) - \Gamma(\phi_l)$  as  $\Delta\Gamma_1$  and  $\Delta\Gamma_2$  for the two metastable states, along with their respective Young's contact angles  $\theta_{Y_1}$  and  $\theta_{Y_2}$ . These represent the dual local stable states due to microscopic roughness on smooth-flat substrates in the context of parabolic wall energy density.  $\theta_{Y_1}$  and  $\theta_{Y_2}$  can be regarded respectively as receding and advancing contact angles as well, and their difference corresponds to the microscopic CAH on smooth-flat substrates.

We then explore how macroscopic roughness influences the local minima states for each initial setting of  $\theta_{Y_1}$  and  $\theta_{Y_2}$ . Given the technical interest in hydrophobic wetting,<sup>71,72</sup> we set  $\Delta\Gamma_1 = -0.2$  with  $\theta_{Y_1} = 101^\circ$  and  $\Delta\Gamma_2 = -0.5$  with  $\theta_{Y_2} = 120^\circ$  for clarity. It is worth mentioning that these settings are accessible via  $180^\circ - \theta_i^*$  in the preceding discussion on microscopic roughness. Consequently, the system energy degenerates into  $E(f, \theta)$ . We analyze the energy landscape of a droplet concerning the contact angle  $\theta$  and the impregnation factor  $f$  in the Cassie–Wenzel state, investigating how macroscopic roughness affects the occurrence of CAH.

The top and bottom panels of Fig. 5 depict the corresponding energy landscape for hydrophobic settings with  $\theta_{Y_1} = 101^\circ$  and  $\theta_{Y_2} = 120^\circ$ , respectively, varying parameter  $\theta$  and impregnation factor  $f \in [0, 1]$ . In Figs. 5(a-1) and (a-2), singular local minima are observed for semicircle profile with  $\theta_1^* = 107^\circ$  and  $f = 0.8$  for  $\theta_{Y_1}$  and  $\theta_2^* = 131^\circ$  and  $f = 0.5$  for  $\theta_{Y_2}$ , indicating the Cassie–Wenzel state. These results align with prior works.<sup>73,74</sup> The semicircle surface profile leads to an increase in contact angle for the hydrophobic wetting setup compared to a smooth-flat substrate. However, this profile only alters the equilibrium value of the contact angle without introducing additional multiple energy minima. Consequently, the competition in the wetting transition employing this profile is governed by microscopic roughness, and the CAH phenomenon for this profile is attributed solely to microscopic roughness.

We enhance the complexity of asperities' roughness by introducing hierarchical variations featuring convex and concave profiles along the vertical direction. Detailed profiles for bottle-shaped and tree-shaped configurations, described by  $\omega(f)$ , are elaborated in Eqs. (17) and (18) using polynomial and sine curves, respectively. In Fig. 5(b-1), the bottle-shaped asperities lead to two energy minima: one border minimum at  $f = 1$  and  $\theta_1^* = 118^\circ$  representing the Wenzel state and another at  $f = 0.2$  and  $\theta_2^* = 127^\circ$  representing the

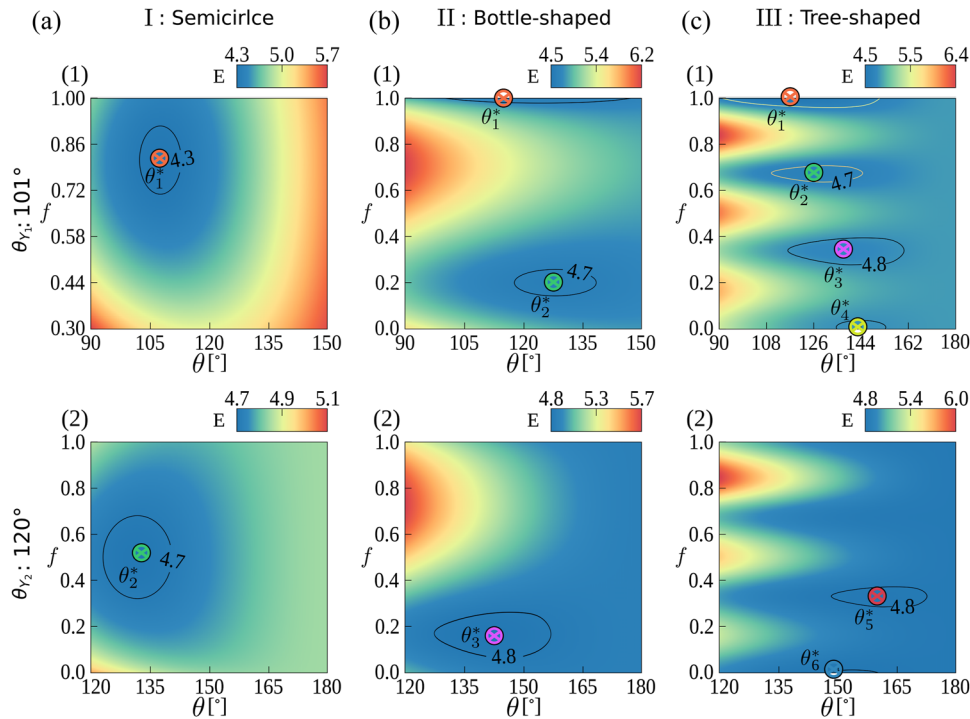


**FIG. 5.** Combined effect of microscopic and macroscopic roughness on CAH. The top and bottom panels depict the corresponding energy landscapes of the system with two hydrophobic wetting setups  $\theta_{Y_1} = 101^\circ$  and  $\theta_{Y_2} = 120^\circ$ . (a) Singular local minimum is observed in Cassie–Wenzel state. Macroscopic roughness increases the stable contact angles with  $\theta_1^* = 107^\circ$  and  $\theta_2^* = 131^\circ$ . (b) and (c) Increasing the complexity of hierarchical roughness in the vertical direction with bumps and grooves leads to more multiple local energy minima. These energy minima correspond to metastable contact angles: bottle-shaped surface profile with  $\theta_i^* \in \{118^\circ, 127^\circ, 141^\circ\}$  and tree-shaped with  $\theta_i^* \in \{117^\circ, 126^\circ, 135^\circ, 143^\circ, 151^\circ, 158^\circ\}$ . The positions of local minima between grooves and bumps indicate the contact line pinning effect.

Cassie–Wenzel state for the  $\theta_{Y_1}$  setup. These findings highlight the capacity of macroscopic roughness to yield multiple energy minima. For  $\theta_{Y_2}$  in Fig. 5(b-2), a single energy minimum at  $f = 0.18$  with  $\theta_3^* = 141^\circ$  in the Cassie–Wenzel state is observed. It is worth noting that for this setup, another minimum exists at the border with  $f = 1$  in the Wenzel state with  $\theta^* = 180^\circ$ , which, mathematically correct though, does not occur in nature. Comparison with the results for  $\theta_{Y_1}$  shows that the presence of a singular energy minimum suggests that macroscopic roughness can augment local energy minima, albeit constrained by inherent hydrophobicity/hydrophilicity. This constraint is further evident in the limitation of introducing macroscopic roughness to increase the number of local energy minima, as seen in Fig. 5(c).

Figure 5(c) demonstrates that increasing complexity with more convex and concave profiles results in multiple energy minima with increasing  $f$  for each setup. Introducing a tree-shaped surface profile as macroscopic roughness increases the number of local energy minima to six from the original dual metastable states  $\theta_{Y_1}$  and  $\theta_{Y_2}$  on smooth-flat substrates. For  $\theta_{Y_1}$  setup, four local stable states are observed:  $\theta_1^* = 117^\circ$  and  $f = 1$ ,  $\theta_2^* = 126^\circ$  and  $f = 0.67$ ,  $\theta_3^* = 135^\circ$  and  $f = 0.34$ , and  $\theta_4^* = 143^\circ$  and  $f = 0$ . The  $\theta_{Y_2}$  setup results in two additional possible metastable states with  $\theta_5^* = 158^\circ$  and  $f = 0.34$  and  $\theta_6^* = 151^\circ$  and  $f = 0$ . Compared with the results from the semicircle surface profile, the tree-shaped surface induces not only larger but also more metastable contact angles. This indicates that the hierarchical roughness stabilizes the hydrophobic state and induces a pinning effect with slightly decreasing contact angles along with increasing  $f$ . The correct local minima position locates at the crest of concave profiles, signifying that alternations in surface curvature stabilize the triple junction, resulting in multiple metastable states

in the vertical position. This aligns with conclusions from previous works.<sup>54,75</sup>

The presence of multiple energy minima in the landscape highlights the active energy needed to overcome the energy barrier between metastable states. Thus, designing surface structures to decrease energy barriers for small  $f$  and enhance them for large  $f$  facilitates droplet rolling easily. Figure 1(b) assumes the existence of multiple local energy minima based on contact angle  $\theta$  variations without explaining their origin in roughness effects. This rough interpretation of multiple energy minima regarding  $\theta$  variations is addressed through systematic discussion in this section, revealing the complexity behind CAH influenced by both microscopic and macroscopic roughness. The details of these influences will be further explored in Sec. III D.

#### D. Contact angle hysteresis

So far, we have demonstrated that both microscopic as well as macroscopic roughness can lead to multiple energy minima in the surface energy system. These multiple energy minima correspond to metastable contact angles, which give rise to CAH. However, as discussed in Sec. III C, the effect of macroscopic roughness on CAH is constrained by both microscopic roughness and its hydrophobicity/hydrophilicity nature. In this section, we will examine how these factors interact and influence CAH. By exploring these mechanisms, we can explain two seemingly contradictory experimental observations: high contact angles with low CAH (referred to as the lotus effect, see Ref. 52) and high contact angles with high CAH (referred to as the rose petal effect, see Ref. 45). For clarity, we divide CAH into three types:

**TABLE I.** CAH induced solely by macroscopic roughness. The table summarizes the effects of varying inherent hydrophobicity ( $\theta_Y$ ) and different macroscopic roughness on CAH (macroscopic CAH).  $\theta_i^*$ <sup>a</sup> denotes the metastable contact angles induced by macroscopic roughness.  $\Delta\theta_{\max}$  represents the maximum CAH caused by macroscopic roughness for each  $\theta_Y$ .

Shape	Semicircle (°)			Bottle (°)			Tree (°)				
	$\theta_Y$ (°)	$\theta_1^*$	$\Delta\theta_{\max}$	$\theta_1^*$	$\theta_2^*$	$\Delta\theta_{\max}$	$\theta_1^*$	$\theta_2^*$	$\theta_3^*$	$\theta_4^*$	$\Delta\theta_{\max}$
90	90	0	90	119	29	90	108	124	138	48	
101	107	0	118	127	9	117	126	135	143	26	
120	131	0	141	\ <sup>b</sup>	0	151	158	\	\	7	
143	156	0	158	\	0	162	\	\	\	0	

<sup>a</sup>  $i \in \mathbb{Z}^+$ .

<sup>b</sup> \ indicates the non-natural limiting case with  $f = 1$  (Wenzel state) but  $\theta = 180^\circ$ .

- Microscopic CAH: hysteresis caused only by microscopic roughness, that is, CAH occurs on smooth-flat and chemically homogeneous surfaces.
- Macroscopic CAH: hysteresis due solely to macroscopic roughness, that is, with microscopic CAH = 0.
- Combined CAH: hysteresis induced by the combined effect of microscopic as well as macroscopic roughness, often observed in reality.

Microscopic CAH has been sufficiently discussed in Sec. III A and is attributed to the arrangement of molecules in multiple metastable states. To analyze the influence of different hydrophobicity/hydrophilicity and macroscopic roughness on CAH, we use a linear wall energy density to describe the microscopic roughness. In this scenario, there exists a single equilibrium contact angle on smooth surfaces, typically referred to as Young's angle ( $\theta_Y$ ). We investigate four groups of distinct  $\theta_Y = \{90^\circ, 101^\circ, 120^\circ, 143^\circ\}$ , with the results summarized in Table I.

From Table I, we obtain the following observations. While semicircle roughness increases the contact angle, it does not induce additional metastable contact angles, meaning no macroscopic CAH

is observed. This suggests that such first-level roughness (e.g., semicircle profile) does not generate macroscopic CAH. Compared to the semicircle roughness, bottle- and tree-shaped roughness cause higher contact angles and induce multiple metastable contact angles, leading to macroscopic CAH. Increasing the complexity of the second-level roughness (i.e., introducing more concave and convex features in asperities) enhances both the contact angles and macroscopic CAH.

In general, high contact angles indicate low affinity between the liquid and solid molecules, while high CAH suggests strong adhesion to the liquid. This contradiction highlights that even with low adhesion between liquid and solid molecules, the introduction of second-level roughness can significantly enhance the adhesion to liquid with high macroscopic CAH. However, this conclusion depends on the level of inherent hydrophobicity. When the inherent hydrophobicity reaches superhydrophobic levels (e.g.,  $\theta_Y = 143^\circ$ ), bottle- and tree-shaped surfaces still increase the contact angle, but no CAH is observed. Across all roughness profiles at this level of hydrophobicity, they all exhibit similar contact angles without CAH. This suggests that at superhydrophobic levels, the low affinity characteristic of intermolecular bonding dominates, and even complex second-level roughness does not increase substrate adhesion to the liquid. In other words, the influence of macroscopic roughness on CAH is contingent upon the inherent hydrophobicity of the substrate. This conclusion is aligned with the work of Bhushan and Her<sup>76</sup>.

Based on the absence of microscopic CAH, we demonstrate that second-level roughness can increase larger contact angles while increasing macroscopic CAH, corresponding to the petal effect. However, in practical observations, small CAH is also often observed for hierarchical roughness structures, corresponding to the so-called lotus effect. For instance, lotus leaf, with such second-level roughness [see Fig. 2(c-1)], exhibits low adhesion to water and excellent self-cleaning ability. At this stage, considering macroscopic CAH alone is insufficient to explain these opposing behaviors for hierarchical roughness. Therefore, we extend our analysis to the combined roughness and CAH. To clarify this, we assume parabolic wall energy density to represent microscopic roughness, which results in

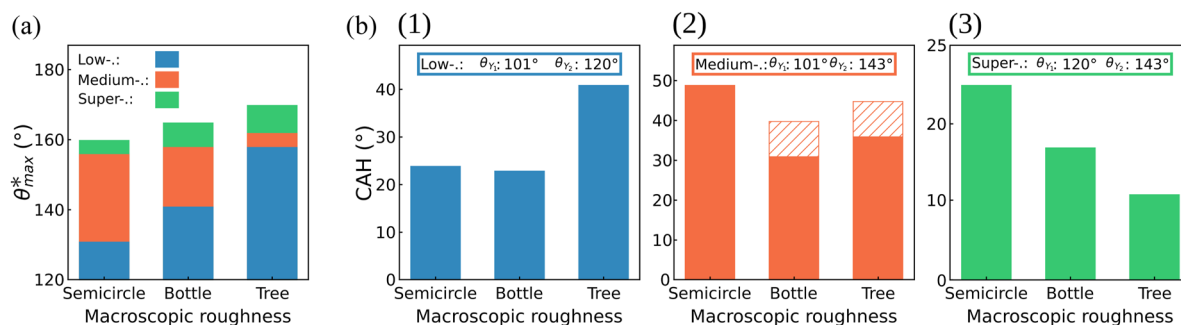


**FIG. 6.** CAH induced by combined roughness. Three groups with distinct microscopic CAH: low (blue), medium (orange), and super (green) hydrophobicity. Increasing roughness complexity: (a) All three groups with larger contact angles. (b)(1) Low-hydrophobicity group with increased CAH (rose petal effect). (b)(2) and (b)(3) Medium- and super-hydrophobicity groups with small CAH (lotus effect). The hatched area in (b)(2) indicates a region of assumed complete immersion into second-level roughness grooves ( $f = 1$ ) with a smaller contact angle, which is unlikely in reality due to the curvature effect and might be neglected.  $\theta_{\max}^*$  denotes the largest induced metastable contact angles within each group.

dual locally stable states with two distinct contact angles on smooth surfaces. The difference between these angles is referred to as microscopic CAH. Without loss of generality, we analyze three groups: low hydrophobicity, medium hydrophobicity, and super hydrophobicity with corresponding contact angles  $\theta_{Y_1} = \{101^\circ, 101^\circ, 120^\circ\}$ , and  $\theta_{Y_2} = \{120^\circ, 143^\circ, 143^\circ\}$ , represented by blue, orange, and green colors, respectively, in Fig. 6.

Figure 6(a) shows that hierarchical roughness leads to higher contact angles across all three groups. However, as depicted in Fig. 6(b), the effect of macroscopic roughness on combined CAH is strongly influenced by microscopic CAH. Specifically, in Fig. 6(b-1), increasing the complexity of roughness by adding more convex and concave profiles along the vertical direction of asperities results in higher CAH for the low-hydrophobicity group, consistent with the rose petal effect. Conversely, for the medium- and super-hydrophobicity groups, increasing roughness complexity causes lower CAH and reduced adhesion, corresponding to the lotus effect, as shown in Figs. 6(b-2) and 6(b-3). The hatched area in the medium-hydrophobicity group suggests that this region may be neglected, as it assumes full droplet immersion into the second-level roughness grooves ( $f = 1$ ) with minimal contact angles. Since our surface energy model does not consider the curvature effect, we assume that the droplet fully immerses into these grooves without resistance. However, achieving complete immersion ( $f = 1$ ) is highly unlikely for hydrophobic liquids, especially when considering the effects of Laplace pressure and air compression. In reality, some air bubbles are likely to be trapped within the grooves of the second-level roughness. Future work is needed to address this limitation by incorporating the effects of curvature and air entrapment. Despite this simplification, our model provides a systematic explanation for the mechanisms contributing to CAH, clarifying the contrasting observations of the lotus effect and the rose petal effect.

#### IV. CONCLUSION

Previous researchers have primarily attributed CAH to macroscopic roughness, which alters the effective interfacial energy through morphological imperfections or chemical heterogeneity of the substrate. In the present work, we demonstrate another origin of CAH at the molecule level: microscopic roughness. Zooming in on the fluid–solid interface, we find that the complex multi-body interactions between fluid and solid molecules determine the variable interfacial tension with multiple minima. By considering the interfacial tension as a function of composition, we develop a mathematical model to explain the CAH phenomenon on chemically homogeneous and smooth-flat substrates, which the Cassie–Wenzel mechanism cannot explain.

In our analyses, the mechanism of microscopic CAH is attributed to molecular rearrangement at the microscopic level. Through diffusion, slip of fluid molecules, or orientation of polar groups, the inhomogeneous fluid–solid interface adjusts its microscopic composition and structures to reach multiple surface energy minima, resulting in microscopic CAH. Our results also complement the current view of multiple local surface energy minima in the droplet–gas–substrate system. We suggest that the system's total surface energy,  $E$ , is influenced by various effects, such as

the complexity of effective molecular interactions or the nonlinear topography of substrates. Therefore,  $E$  should be studied as a multi-variable function rather than a single-variable function dependent only on the contact angles,  $\theta$ . Furthermore, we emphasize that the microscopic mechanism can be extended to include macroscopic roughness effects. By combining microscopic and macroscopic roughness, more surface energy minima appear, leading to more complex CAH phenomena. Investigating the contrasting wetting behaviors (the lotus effect vs the rose petal effect) due to combined roughness reveals the multifaceted mechanisms underlying CAH.

In conclusion, we argue that CAH involves not only the effective contact area change by droplet receding and advancing on the macroscale but also molecular rearrangements at the microscopic level. Both mechanisms are crucial for the origin of CAH. In addition, rearrangement can be heavily influenced by external fields such as temperature, mechanical force, and electrostatic interactions. So our model can elucidate more complex scenarios by incorporating these external fields into the fluid–solid interactions at the interface, allowing for the study of phenomena such as electro-wetting and adaptive wetting. It is important to note that the combined roughness model neglects the curvature effect at the liquid–gas interface beneath the droplet, as well as the immersed volume of liquid within the grooves. In addition, the spatial relationship between the height of asperities and their periodicity on the substrate significantly impacts CAH and warrants further investigation in future work.

As CAH on smooth-flat substrates is associated with varying interfacial tension, our model may also inform future experiments on measuring interfacial tension through CAH. The combined CAH mechanism we have elucidated provides valuable insights that could guide researchers in the design of functional surfaces. We hope our findings provide a new perspective on CAH in various fields.

#### SUPPLEMENTARY MATERIAL

The [supplementary material](#) document presents the variations of the CAH phenomenon on a chemically homogeneous and smooth-flat substrate with linear, cubic, and double-well wall energy density formulations, respectively.

#### ACKNOWLEDGMENTS

This research was supported by the German Research Foundation (DFG) in the frame of the Research Training Group 2561: Materials Compounds from Composite Materials, the Gottfried-Wilhelm Leibniz prize Grant No. NE 822/31-1 of the German Research Foundation (DFG), and the VirtMat project “VirtMat P09: Wetting Phenomena” of the Helmholtz association within the MSE Program No. 43.31.01.

#### AUTHOR DECLARATIONS

##### Conflict of Interest

The authors have no conflicts to disclose.

## Author Contributions

**Hongmin Zhang:** Conceptualization (supporting); Formal analysis (lead); Investigation (lead); Methodology (lead); Validation (lead); Visualization (lead); Writing – original draft (lead); Writing – review & editing (lead). **Haodong Zhang:** Conceptualization (supporting); Formal analysis (supporting); Investigation (supporting); Supervision (equal); Validation (equal); Visualization (equal); Writing – original draft (lead); Writing – review & editing (lead). **Fei Wang:** Conceptualization (lead); Methodology (supporting); Supervision (supporting); Validation (supporting); Writing – review & editing (supporting). **Britta Nestler:** Funding acquisition (lead); Project administration (lead); Supervision (lead); Validation (supporting); Writing – original draft (supporting); Writing – review & editing (supporting).

## DATA AVAILABILITY

The data that support the findings of this study are available within the article and its [supplementary material](#).

## REFERENCES

- 1 T. Young, *Philos. Trans. R. Soc. London* **95**, 65 (1805).
- 2 D. Seveno, T. D. Blake, and J. De Coninck, *Phys. Rev. Lett.* **111**, 096101 (2013).
- 3 N. Tretyakov, M. Müller, D. Todorova, and U. Thiele, *J. Chem. Phys.* **138**, 064905 (2013).
- 4 J. D. Andrade, L. M. Smith, and D. E. Gregonis, *Surface and Interfacial Aspects of Biomedical Polymers: Volume 1 Surface Chemistry and Physics* (Plenum Press, New York and London, 1985), Vol. 249.
- 5 G. Whyman, E. Bormashenko, and T. Stein, *Chem. Phys. Lett.* **450**, 355 (2008).
- 6 J. Y. Kim, S. Heyden, D. Gerber, N. Bain, E. R. Dufresne, and R. W. Style, *Phys. Rev. X* **11**, 031004 (2021).
- 7 M. A. Van Limbeek, M. H. Essink, A. Pandey, J. H. Snoeijer, and S. Karpitschka, *Phys. Rev. Lett.* **127**, 028001 (2021).
- 8 C. Yan, D. Guan, Y. Wang, P.-Y. Lai, H.-Y. Chen, and P. Tong, *Phys. Rev. Lett.* **132**, 084003 (2024).
- 9 Y. Sun, C. J. Radke, B. D. McCloskey, and J. M. Prausnitz, *J. Colloid Interface Sci.* **529**, 582 (2018).
- 10 E. Arzt, H. Quan, R. M. McMeeking, and R. Hensel, *Prog. Mater. Sci.* **120**, 100823 (2021).
- 11 R. Seemann, M. Brinkmann, T. Pfohl, and S. Herminghaus, *Rep. Prog. Phys.* **75**, 016601 (2011).
- 12 D. Tian, Y. Song, and L. Jiang, *Chem. Soc. Rev.* **42**, 5184 (2013).
- 13 H.-J. Butt, J. Liu, K. Koynov, B. Straub, C. Hinduja, I. Roismann, R. Berger, X. Li, D. Vollmer, W. Steffen, and M. Kappl, *Curr. Opin. Colloid Interface Sci.* **59**, 101574 (2022).
- 14 R. Seemann, M. Brinkmann, E. J. Kramer, F. F. Lange, R. Lipowsky, and R. Lipowsky, *Proc. Natl. Acad. Sci. U. S. A.* **102**, 1848 (2005).
- 15 E. Bormashenko, *Adv. Colloid Interface Sci.* **222**, 92 (2015).
- 16 N. A. Patankar, *Langmuir* **20**, 7097 (2004).
- 17 A. Cassie, *Discuss. Faraday Soc.* **3**, 11 (1948).
- 18 E. Chibowski, *Adv. Colloid Interface Sci.* **103**, 149 (2003).
- 19 C. W. Extrand, *J. Colloid Interface Sci.* **248**, 136 (2002).
- 20 P. Rahimi and C. Ward, *Microgravity Sci. Technol.* **16**, 231 (2005).
- 21 Y. Chen, C. Helm, and J. Israelachvili, *J. Phys. Chem.* **95**, 10736 (1991).
- 22 C. W. Extrand and Y. Kumagai, *J. Colloid Interface Sci.* **191**, 378 (1997).
- 23 K.-Y. Law, *Acc. Mater. Res.* **3**(1), 1–7 (2021).
- 24 F. Wang, B. Nestler *et al.*, *Phys. Rev. Lett.* **132**, 126202 (2024).
- 25 B. Neirinck, D. Soccol, J. Fransaer, O. V. d. Biest, and J. Vleugels, *J. Colloid Interface Sci.* **348**, 654 (2010).
- 26 A. Contreras, *J. Colloid Interface Sci.* **311**, 159 (2007).
- 27 Y.-T. Cheng, K.-C. Chu, H.-K. Tsao, and Y.-J. Sheng, *J. Colloid Interface Sci.* **578**, 69 (2020).
- 28 A. Ghoufi, P. Malfreyt, and D. J. Tildesley, *Chem. Soc. Rev.* **45**, 1387 (2016).
- 29 H. Zhang, Y. Wu, F. Wang, and B. Nestler, *J. Chem. Phys.* **159**, 164701 (2023).
- 30 G. Le Breton and L. Joly, *J. Chem. Phys.* **152**, 241102 (2020).
- 31 E. Bormashenko, *J. Colloid Interface Sci.* **537**, 597 (2019).
- 32 N. Eustathopoulos, *Acta Mater.* **46**, 2319 (1998).
- 33 N. Eustathopoulos, *Metals* **5**, 350 (2015).
- 34 C. Ward and J. Wu, *Phys. Rev. Lett.* **100**, 256103 (2008).
- 35 B. H. Tan, H. An, and C.-D. Ohl, *Phys. Rev. Lett.* **130**, 064003 (2023).
- 36 V. Starov, *Colloid Polym. Sci.* **291**, 261 (2013).
- 37 I. Kuchin and V. Starov, *Langmuir* **31**, 5345 (2015).
- 38 F.-C. Wang and Y.-P. Zhao, *Colloid Polym. Sci.* **291**, 307 (2013).
- 39 T. D. Blake, J.-C. Fernandez-Toledano, G. Doyen, and J. De Coninck, *Phys. Fluids* **27**, 112101 (2015).
- 40 A. Nold, D. N. Sibley, B. D. Goddard, and S. Kalliadasis, *Phys. Fluids* **26**, 072001 (2014).
- 41 A. P. Hughes, U. Thiele, and A. J. Archer, *J. Chem. Phys.* **142**, 074702 (2015).
- 42 Y. Deng, L. Chen, Q. Liu, J. Yu, and H. Wang, *J. Phys. Chem. Lett.* **7**, 1763 (2016).
- 43 C. Radke, *Adv. Colloid Interface Sci.* **222**, 600 (2015).
- 44 A. I. Rusanov, *Surf. Sci. Rep.* **23**, 173 (1996).
- 45 B. Bhushan and M. Nosonovsky, *Philos. Trans. R. Soc., A* **368**, 4713 (2010).
- 46 L. D. Landau and E. M. Lifshitz, *Statistical Physics* (Elsevier, 2013), Vol. 5.
- 47 J. W. Cahn and J. E. Hilliard, *J. Chem. Phys.* **28**, 258 (1958).
- 48 J. W. Cahn, *J. Chem. Phys.* **66**, 3667 (1977).
- 49 H. Hardy, *Acta Metall.* **1**, 202 (1953).
- 50 E. Guggenheim, *Trans. Faraday Soc.* **33**, 151 (1937).
- 51 P.-G. De Gennes, *Rev. Mod. Phys.* **57**, 827 (1985).
- 52 K. Koch, B. Bhushan, Y. C. Jung, and W. Barthlott, *Soft Matter* **5**, 1386 (2009).
- 53 D. Gandyra, S. Walheim, S. Gorb, P. Ditsche, W. Barthlott, and T. Schimmel, *Small* **16**, 2003425 (2020).
- 54 N. Michael and B. Bhushan, *Microelectron. Eng.* **84**, 382 (2007).
- 55 F. Wang, Y. Wu, and B. Nestler, *Adv. Mater.* **35**, 2210745 (2023).
- 56 A. Ahmed, R. Sanedrin, T. Willers, and P. R. Waghmare, *J. Colloid Interface Sci.* **608**, 1086 (2022).
- 57 T. Smith and G. Lindberg, *J. Colloid Interface Sci.* **66**, 363 (1978).
- 58 C. Andrieu, C. Sykes, and F. Brochard, *Langmuir* **10**, 2077 (1994).
- 59 F. M. Ruiz-Cabello, M. Rodríguez-Valverde, and M. Cabrerizo-Vilchez, *Adv. Colloid Interface Sci.* **206**, 320 (2014).
- 60 J. W. Drelich, L. Boinovich, E. Chibowski, C. Della Volpe, L. Holysz, A. Marmur, and S. Siboni, *Surf. Innovations* **8**, 3 (2020).
- 61 L. Girifalco and R. J. Good, *J. Phys. Chem.* **61**, 904 (1957).
- 62 M. L. Huggins, *J. Chem. Phys.* **9**, 440 (1941).
- 63 P. J. Flory, *J. Chem. Phys.* **10**, 51 (1942).
- 64 J.-W. Song and L.-W. Fan, *Adv. Colloid Interface Sci.* **288**, 102339 (2021).
- 65 M. Tadros, P. Hu, and A. Adamson, *J. Colloid Interface Sci.* **49**, 184 (1974).
- 66 G. Heydari, M. S. Moghaddam, M. Tuominen, M. Fielden, J. Haapanen, J. M. Mäkelä, and P. M. Claesson, *J. Colloid Interface Sci.* **468**, 21 (2016).
- 67 A. Terzis, E. Roumeli, K. Weishaupt, S. Brack, H. Aslannejad, J. Groß, S. Hassanizadeh, R. Helmig, and B. Weigand, *J. Colloid Interface Sci.* **504**, 751 (2017).
- 68 M. E. Diaz, M. D. Savage, and R. L. Cerro, *J. Colloid Interface Sci.* **503**, 159 (2017).
- 69 G. Nam and S.-H. Yoon, *J. Colloid Interface Sci.* **556**, 503 (2019).

<sup>70</sup>H.-J. Butt, R. Berger, W. Steffen, D. Vollmer, and S. A. Weber, *Langmuir* **34**, 11292 (2018).  
<sup>71</sup>T. L. Liu and C.-J. C. Kim, *Science* **346**, 1096 (2014).  
<sup>72</sup>F. Geyer, M. D'Acunzi, A. Sharifi-Aghili, A. Saal, N. Gao, A. Kaltbeitzel, T.-F. Slood, R. Berger, H.-J. Butt, and D. Vollmer, *Sci. Adv.* **6**, eaaw9727 (2020).

<sup>73</sup>A. Marmur, *Langmuir* **19**, 8343 (2003).  
<sup>74</sup>S. Herminghaus, M. Brinkmann, and R. Seemann, *Annu. Rev. Mater. Res.* **38**, 101 (2008).  
<sup>75</sup>M. Sun, C. Luo, L. Xu, H. Ji, Q. Ouyang, D. Yu, and Y. Chen, *Langmuir* **21**, 8978 (2005).  
<sup>76</sup>B. Bhushan and E. K. Her, *Langmuir* **26**, 8207 (2010).